metals

MDPI

Article

Effect of Cladding Current on Microstructure and Wear Resistance of High-Entropy Powder-Cored Wire Coating

Xinghai Shan [1], Mengqi Cong [2,*] and Weining Lei [1]

[1] School of Mechanical Engineering, Jiangsu University of Technology, Changzhou 213001, China
[2] Key Laboratory of Advanced Materials Design and Additive Manufacturing of Jiangsu Province, Jiangsu University of Technology, Changzhou 213001, China
* Correspondence: congmq@jsut.edu.cn

Abstract: This paper investigated the effect of tungsten arc melting current on the microstructure and wear resistance of coatings prepared from high-entropy powder-cored wire, $FeCrMnCuNiSi_1$. A powder-cored wire of high-entropy composition was drawn by powder-cored wire-forming equipment, and a $FeCrMnCuNiSi_1$ high-entropy alloy coating was designed on the base material 40Cr by the tungsten arc fusion technique. The influence law and mechanism of melting current on the wear resistance of the coatings were obtained through analyzing the microstructure, physical phase, and wear resistance of the coatings prepared by different melting currents. At a melting current of 200A, the $FeCrMnCuNiSi_1$ coating exhibits fine equiaxed grains and a single BCC phase; the highest and average microhardness of the coating reach 790.36 HV and 689.73 HV, respectively, whose average microhardness is twice that of the base material. The wear rate of the coating is 2245.86 $\mu m^3/(N \cdot \mu m)$, which is only 8% of the base material and has excellent wear resistance. The $FeCrMnCuNiSi_1$ high-entropy alloy coating prepared by ordinary powder-cored wire-forming equipment and the tungsten arc cladding method has excellent performance and low cost, which can provide an essential basis for the development, preparation, and application of high-entropy alloy coatings.

Keywords: coating; high-entropy alloy; tungsten arc; fatigue wear; abrasive wear; adhesive wear

Citation: Shan, X.; Cong, M.; Lei, W. Effect of Cladding Current on Microstructure and Wear Resistance of High-Entropy Powder-Cored Wire Coating. *Metals* **2022**, *12*, 1718. https://doi.org/10.3390/met12101718

Academic Editor: Eduard Hryha

Received: 16 August 2022
Accepted: 9 October 2022
Published: 14 October 2022

1. Introduction

While conventional alloys have been endowed with various desirable properties, usually by adding relatively few minor elements to the major ones, high-entropy alloys break with this concept and consist of high concentrations of multiple major elements [1]. In 2004, Yeh et al. [2] and Cantor et al. [3] introduced the concepts of high-entropy alloys and isotonic ratio multicomponent alloys, respectively, which are alloyed materials composed of five or more significant elements with atomic fractions ranging from >5% to <35% of each central element. The high-entropy alloy thermodynamically exhibits a lower Gibbs free energy because of its mixed state with multiple primary elements. The microstructure of high-entropy alloys mainly consists of face-centered cubic (FCC), body-centered cubic (BCC), HCP (dense hexagonal), and a few compounds generated from mixed elements. The alloys have some excellent properties that are incomparable to traditional alloys, such as high strength [4], high wear resistance [5], corrosion resistance [6], high tensile strength [7], and resistance to oxidation at high temperatures [8]. Therefore, high-entropy alloys have become hot spots for research as coatings applied to the surface modifications of steel, aluminum alloys, and other materials.

At present, the preparation methods of high-entropy alloys mainly include vacuum arc melting [9], induction arc melting [10], mechanical alloying [11], and magnetron sputtering [12]. However, these methods have the problems of a complex production process and high preparation costs. Therefore, the coating preparation method with simple operation

and low manufacturing cost has attracted the attention of production practices, such as laser cladding [13], electron beam melting [14], plasma arc deposition [15], and tungsten arc cladding [16]. For example, Zoia Duriagina et al. used laser alloying and plasma chemical vapor deposition to prepare coatings with excellent performance on stainless steel [17,18]. In these coating preparation methods, tungsten arc cladding has the characteristics of low equipment cost, easy operation, and comprehensive application scenarios. In addition, due to the cladding process, the tungsten needle does not melt and the discharge arc length changes relatively few disturbing factors, as well as the welding process is stable and the whole process is filled with the inert shielding gas argon, which forms a good airflow isolation layer that effectively prevents oxygen and nitrogen from equaling the coating development into a chemical reaction; thus, the prepared coating has better fusion with the substrate, which has received much attention from researchers. Shen et al. [19] prepared cable-type filaments. They used a tungsten arc to prepare a bulk AlCoCrFeNi high-entropy alloy with no defects in the microstructure of FCC and BCC; its compressive strength reached 2.9 GPa, and its elongation reached 42%. Dong et al. [20] prepared their powder bed on an arc cladding platform to place the proportioned high-entropy alloy powder, which prevents the protective gas from blowing away the preplaced powder. The high-entropy alloy $AlCoCrFeNi_{2.1}$ prepared by this device has a good combination of tensile strength (719 MPa) and flexibility (27%), with a pseudo-eutectic microstructure consisting of micro phases of more significant FCC phase columnar grains (90 wt%) and a refined BCC phase (10 wt%). Fan et al. [21] investigated the preparation of high-entropy alloy coatings by ultrasound-assisted tungsten arc melting. The average grain diameter of the coatings was reduced from 285 μm to 78 μm, which was refined by 70% under the ultrasonic treatment. The microhardness was increased by 20%, which increased from 441 HV to 532 HV. The optimization of the properties of the high-entropy alloy originated from the grain refinement after the cavitation effect of the ultrasonic treatment. When a high-entropy alloy coating is prepared by arc fusion coating, there are still problems, such as the large diameter of the stranded wire, which cannot be satisfied by existing automatic wire-feeding equipment, significant burn loss during the prefabricated powder fusion coating process, and poor coating formability.

To avoid the above defects in preparing high-entropy alloy coatings by the arc melting method, a new high-entropy powder-cored wire material, $FeCrMnCuNiSi_1$, was developed independently. A commonly used component configuration, 40Cr steel, which has good mechanical properties and welding fusion performance, is used for the base material. The high-entropy alloy coating was prepared using a tungsten arc platform and an automatic wire-feeding device. This method effectively avoids the preset powder being blown away by the protective gas during the melting process. In addition, the automatic wire-feeding device can accurately feed the wire to prepare a high-entropy alloy coating with a controlled thickness. At the same time, the microstructure and mechanical properties of the high-entropy alloy coatings were further investigated, which could provide new ideas and ways to prepare a new high-entropy alloy coating.

2. Materials and Methods

Figure 1 shows a schematic diagram of the process of the $FeCrMnCuNiSi_1$ high-entropy alloy coating. Firstly, according to the design concept of the high-entropy alloy isotonic ratio, the configured alloy powder is placed into a ball mill tank with an appropriate ball material ratio for uniform mixing, and the ball mill tank is filled with the protective gas argon to prevent a chemical reaction of the alloy powder during the ball milling process. Then, the mechanically mixed alloy powder is filtered and dried, followed by placing it in the hopper of the powder-cored wire-forming equipment. A 304 stainless steel strip is rolled into a U-shaped open tube by the forming roller on the powder-cored wire-forming equipment. Finally, the U-shaped open tube is covered with mixed powder, and the welding wire with the specified diameter is obtained through cold rolling, tube rolling, and wire drawing. A 40Cr is used as the substrate material, with a size of 200 mm × 200 mm ×

10 mm. Before melting, the surface of the substrate should be sanded clean with 400- and 800-purpose sandpaper to remove any oil and rust, which can improve the fusion effect of the coating and the substrate. Meanwhile, the platform surface of the arc table should be flat to ensure good conductivity. The optimal high-entropy alloy coatings prepared by the powder-cored wire $FeCrMnCuNiSi_1$ were explored by adjusting the parameters of the melting current. The parameters of the arc cladding were as follows: the shielding gas argon was 15 L/min, the working voltage was 10 V, the arc length was 4 mm, the automatic wire-feeding speed was 150 mm/min, and the cladding currents were 200 A, 220 A, and 240 A, respectively.

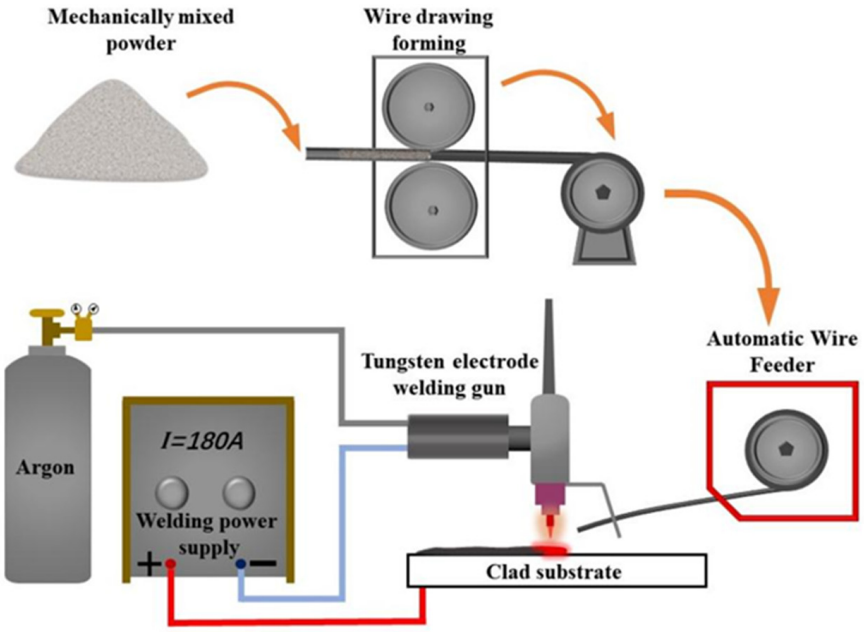

Figure 1. Schematic diagram of the process of the $FeCrMnCuNiSi_1$ high-entropy alloy coating.

The specimens with sizes of 10 mm × 10 mm and 20 mm × 20 mm were cut from the molten coating by an SG3000 EDM machine for surface microstructure characterization and mechanical property testing. The cutting specimen was polished and cleaned by an ultrasonic cleaner, followed by being corroded with a corrosive acid (HNO_3:HCl = 1:3) for 10 s. The above operation was repeated for the specimens with a size of 20 mm × 20 mm, but without a corrosion treatment.

A metallurgical microscope and a SIGMA500 type field-emission scanning electron microscope were used for observing the microstructure before and after the corrosion treatment. The phase analysis of the coatings was analyzed by an HD-Xpretty PRO type X-ray diffractometer with operating parameters of 40 KV and 20 mA and a scanning speed of 5°/min. An HVS-1000A hardness tester was used to test the microhardness of the coating with an applied load of 200 gf and a holding time of 15 s. The wear resistance of the coating was tested for 10 min by an MDW-02 high-speed reciprocating friction and a wear tester with a load of 50 N and a frequency of 10 Hz. A Si_3N_4 with a diameter of 6 mm was used as the grinding ball. The wear volume was calculated. Furthermore, the wear surface morphology and profile were further observed by a Naonvea PS50 3D profiler to investigate the wear mechanism of the coating.

3. Results and Discussion

3.1. Microstructure Characterization

Figure 2 shows the optical micrographs of the $FeCrMnCuNiSi_1$ coating by tungsten arc melting at different currents. Figure 2a–c show the morphology of the coating at three current parameters (200 A, 220 A, and 240 A), all of which exhibit good cross-sectional

profiles with no pores or cracks. Different microstructure characteristics of the region [A] near the fusion line can be observed cleanly in Figure 2(a_1,b_1,c_1). The microstructure of the fusion line between the coating and the substrate exhibits a columnar grain morphology, and the columnar crystals extend to the substrate. Because the substrate subjacent to the melt pool conducts heat as the heat dissipates during the melting, a large number of heterogeneous nucleation are formed under the temperature gradient. Cubic crystals with the orientation of <001> produce epitaxial solidification and fast growth, while other grain growth is hindered. Thus, the coarse columnar grains of the region [A] near the fusion line gradually become larger with the increasing current, which is consistent with the grain forming characteristics of the arc fusion zone and coating [22].

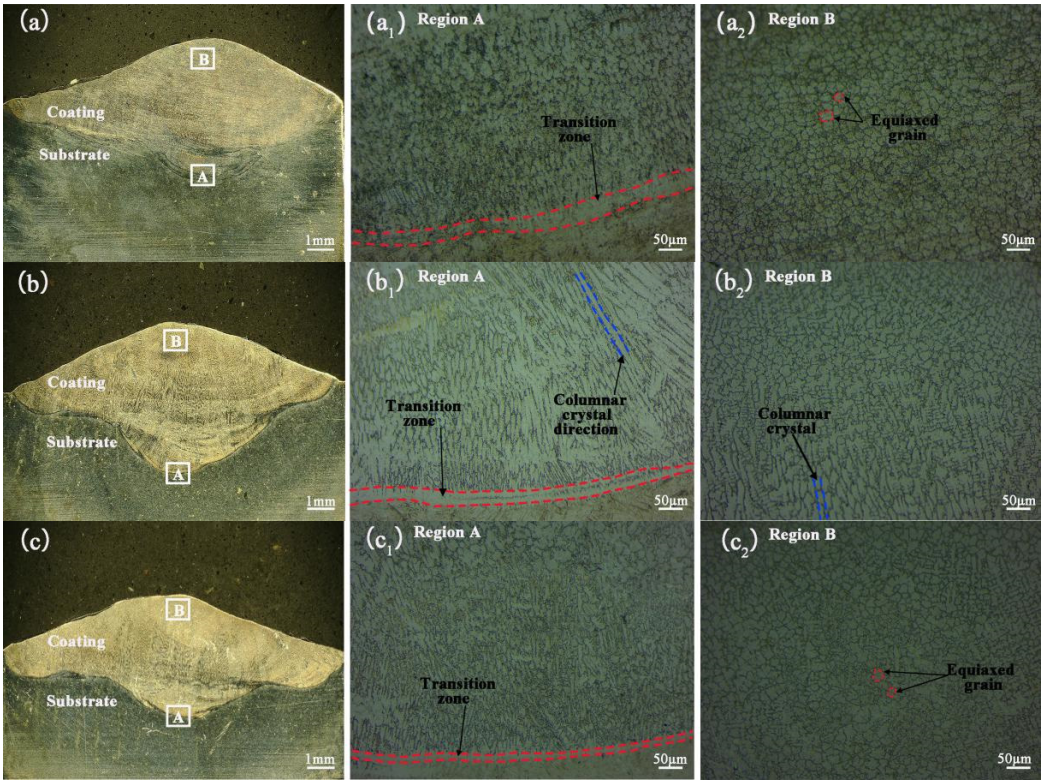

Figure 2. Optical micrographs of the coatings on the FeCrMnCuNiSi$_1$ powder-cored wire at different cladding currents. (**a**,**a$_1$**,**a$_2$**) 200 A; (**b**,**b$_1$**,**b$_2$**) 220 A; (**c**,**c$_1$**,**c$_2$**) 240 A.

The top region [B] of the coating in Figure 2a and c is a more uniform equiaxed crystal structure, while the top region [B] in Figure 2b is a columnar crystal growing by means of dendritic growth. The top of the coating shows a mixture of refined equiaxed and columnar crystals at a melting current of 240 A. The increase in melting current at a constant melting speed leads to a widening at the bottom of the melt pool and an increase in the contact area between the melt pool and the substrate, which increases the ability of the dissipated heat from the melt pool to the substrate and the gradual refinement of grains at the fusion line [23].

The microstructure of the medium-axis and columnar crystals at different melting currents and the typical dendrite microstructure (DR) and interdendritic microstructure (ID) were further observed through scanning electron microscopy, as shown in Figure 3. According to the EDS analysis of the elemental content of the dendritic and interdendritic tissues inside the coating obtained in Table 1, it was found that the elemental content of Fe in the interdendritic tissues is higher than that in the dendritic tissues. The Fe element does not affect the solid solution phase and microstructure, which is significantly higher than the nominal value of the high-entropy alloy due to the dilution effect of the base material.

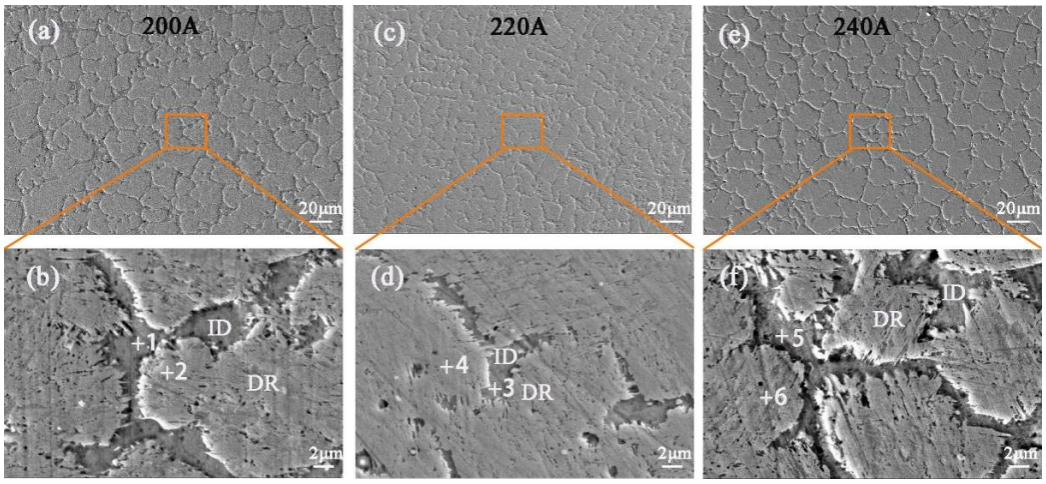

Figure 3. (**a**,**c**,**e**) show the SEM of the top of $FeCrMnCuNiSi_1$ high-entropy alloy coating at melting currents of 200 A, 220 A, and 240 A, respectively. (**b**,**d**,**f**) show the enlarged views of the orange rectangular areas in (**a**,**c**,**e**).

Table 1. EDS of the microstructure of the top region of the $FeCrMnCuNiSi_1$ high-entropy alloy coating at different melting currents.

Coating	Point	Fe	Cr	Mn	Cu	Ni	Si
200 A	1	41.8	17.4	13.9	10.2	13.5	1.1
	2	54.2	13.7	11.6	8.4	10.2	0.6
220 A	3	63.6	9.8	8.8	5.6	8.4	1.9
	4	68.7	7.8	8.2	4.3	8.1	1.4
240 A	5	52.9	15.2	13.5	7.5	8.6	1.0
	6	62.5	10.1	10.0	6.7	8.3	0.9

The Cr elements are mainly in the interdigitated dendritic region, and the ease of the Cr element deviation may be due to its relatively low migration activation energy [24–26]. At the same time, the Cr element can promote the generation of a BCC solid solution, and the hardness and strength of the coating may be reduced due to the decrease in the Cr element content by increasing the current. The relative content of the Cu element is low at 220 A and 240 A. Combined with the analysis in Figure 3b, the melt pool temperature is high, and the amount of Cu element burned is severe due to the higher current, the slower heat dissipation, and the smaller contact area between the melt pool and the base material. It can be observed from Figure 3d that there is a small area of interdendritic tissue. The EDS results in Table 1 show that the elemental content of the dendritic tissue and interdendritic tissue of the columnar crystal is relatively uniform and the elemental segregation is relatively tiny.

3.2. Phase Constitution

Figure 4 shows the XRD patterns of the $FeCrMnCuNiSi_1$ high-entropy alloy coatings with different currents. The XRD patterns show that the $FeCrMnCuNiSi_1$ coating exhibits a BCC phase at 44.76°, 65.15°, and 82.52° with a lattice constant of 2.868 Å, which is basically the same as the α-Fe or $CrFe_4$ lattice constants (λ = 2.866 Å, PDF#87-0721; λ = 2.866 Å, PDF#65-7251). The α-Fe or $CrFe_4$ phases are formed by the A2 (W-type, disordered BCC) structure and B2 (β'-CuZn-type, ordered BCC) structure, respectively [27]. For the FCC diffraction peak at 51.15°, the dot constant of 10.093 Å is the same as that of $Fe_5Ni_4S_8$ (λ = 10.093 Å, PDF#86-2470). The diffraction peak of the coating at a melting current of 200 A exhibits a single BCC structure. The coating prepared at 220 A exhibits the FCC phase. It can also be found that the angle of the FCC phase diffraction peak gradually widens with the increase in the cladding current, which is due to the rise in the cladding

current and the increase in the melt pool temperature. The Ni element, which has a high melting point in the powder-cored wire, reacts with the small amount of Si element in the base material to produce $Fe_5Ni_4S_8$ with a high melting point. The grain size of the coating was calculated by the Debye–Scherrer formula. With the increase in the current from 200 A to 240 A, the grain sizes at the orientation (110) were 15.31, 15.52, and 16.28 nm, respectively, and the grain sizes at the direction (400) were 0, 15.31, and 16.21 nm, respectively. Thus, the grain size of the coating increases with the increase in the current, which verifies the phenomenon that the grain shape becomes more significant with the rise in current in the optical micrograph.

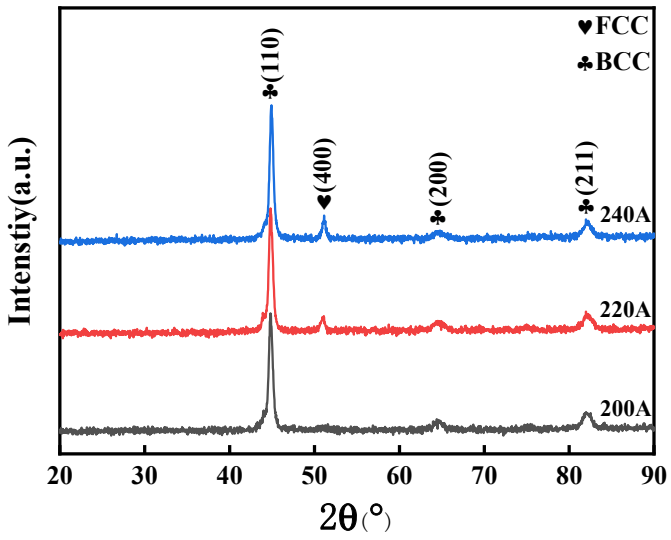

Figure 4. XRD patterns of the $FeCrMnCuNiSi_1$ high-entropy alloy coatings with different currents.

3.3. Mechanical Properties

3.3.1. Microhardness

Figure 5 shows the cross-sectional microhardness results of the coatings at different melting currents. The histograms and line graphs show the average microhardness and microhardness values at each test point on the coating and the substrate, respectively. The histogram shows that the average microhardness of the base material 40Cr is 343.62 HV. The coating has the highest average microhardness of 689.73 HV at a melting current of 200 A, which is twice the average hardness of the base material. It is obvious from the line graph that the microhardness of the coating with the increasing current has a decreasing trend. Because the internal temperature of the melt pool increases sharply, the contact area between the melt pool and the substrate decreases, and the cooling rate of the coating decreases sharply with the increasing current, which results in a larger grain size of the coating. According to the Hall–Patch formula, the grain size increases and the strength and hardness decrease [28]. Additionally, the coatings at the melting currents of 220 A and 240 A have a lower content of non-metallic Si elements, which will improve the plasticization of the coatings and reduce their hardness. The coatings at these two currents derive from FCC phases and have a lower content of non-metallic Si elements; FCC phases and Si elements in high-entropy alloys can improve the plasticization; thus, the hardness decreases due to the combined effect of grain size, FCC, and Si elements. The coating has the lowest average microhardness when the melting current is 220 A. The coating at the melting current of 220 A exhibits a columnar crystal structure, which has a lower Cr segregation compared to the equiaxed crystals, resulting in the lowest strength and hardness. It can also be observed that the maximum hardness of the coatings appears at the top of the coating, which is due to the diffusion strengthening effect through the refinement of the grain microstructure in the top region. At the same time, the fusion lines are mostly coarse columnar crystals extending toward the base material, which leads to the lowest hardness [29].

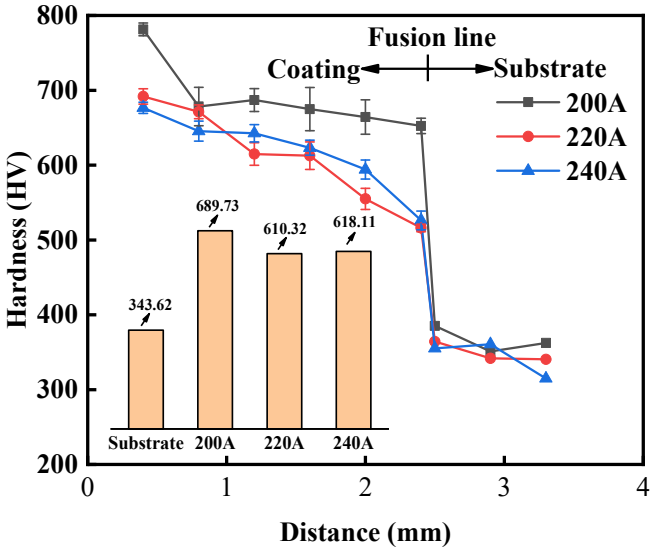

Figure 5. Cross-sectional microhardness of the $FeCrMnCuNiSi_1$ high-entropy alloy coatings with different currents.

3.3.2. Abrasion Resistance

Figure 6 shows the 3D profiles of the wear tracks for the base material and the high-entropy alloy coating at different melting currents. It can be observed that the wear track in the base material is much wider than that of the high-entropy alloy coating. Combined with the color scale on the right side in Figure 6, it is found that the wear track of the base material is much deeper than that of the coating. The data in Table 2 can be obtained by analyzing the 3D profiles. The wear tracks of the coatings reach a wear depth of 11.6, 18.4, and 15.5 μm at the melting current of 200 A, 220 A, and 240 A, respectively. The cross-sectional areas of the coating wear tracks were 4133, 7791, and 4052 μm^2, respectively. The wear was most serious at the melting current of 220 A, but its depth was only 1/5 of the cross-sectional area of the base material. The wear resistance of the coating can be compared quantitatively by the wear rate, which Equation (1) shows as follows:

$$\delta = V/\Sigma W, \quad (1)$$

$$Q = KWL/H, \quad (2)$$

(1) where V is the wear volume, and ΣW is the accumulated work done by friction;
(2) where Q is the material wear volume, K is the friction coefficient, W is the normal load, L is the sliding length, and H is the material surface hardness.

Table 2. Wear resistance test results of the base material and the high-entropy alloy coating of $FeCrMnCuNiSi_1$ with different melting currents.

Sample	Maximum Wear Depth μm	Wear Cross-Sectional Area μm^2	Wear Rate $\mu m^3/(N \cdot \mu m)$
40Cr	52.5	39,765	26,984.86
200 A	11.6	4133	2999.76
220 A	18.4	7791	6168.82
240 A	15.5	4052	2245.86

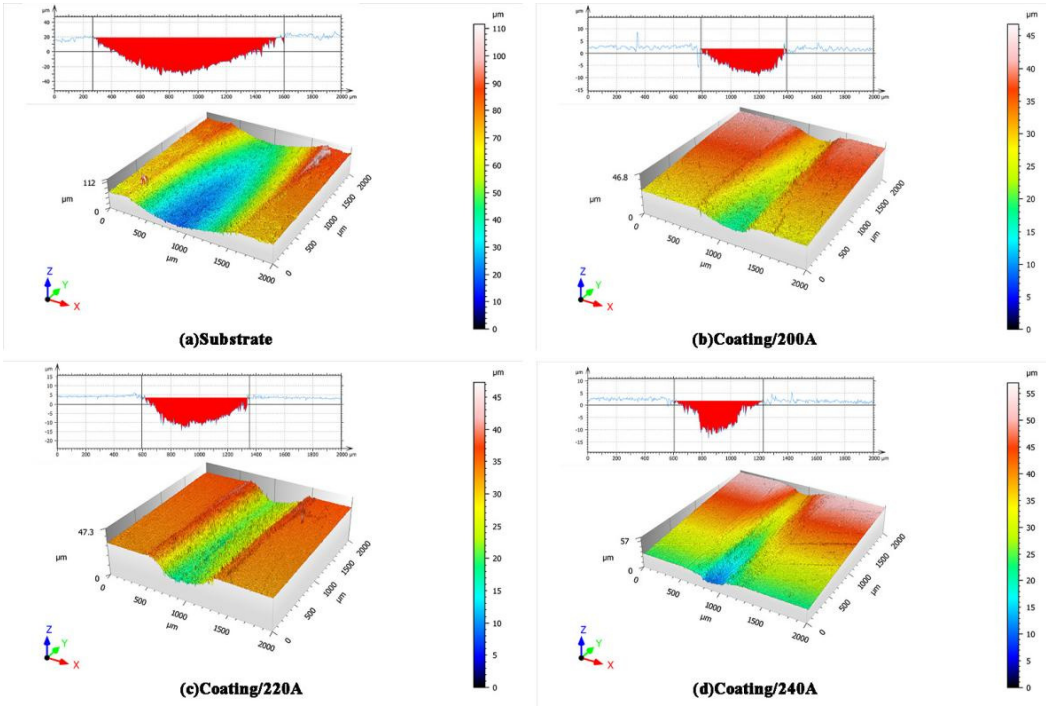

Figure 6. (**a**) 3D view and cross-sectional view of the abrasion marks of the base material. (**b**–**d**) 3D view and cross-sectional view of the abrasion marks of the FeCrMnCuNiSi$_1$ high-entropy alloy coating with different melting currents.

The wear rate, which is obtained from Equations (1) and (2), at the melting current of 200 A, 220 A, and 240 A is 2999.76 μm^3/(N·μm), 6168.82 μm^3/(N·μm), and 2245.86 μm^3/(N·μm), respectively. It can be observed that the maximum wear rate is only 22% of the base material wear rate. From the above analysis, the coating has the lowest average microhardness when the melting current is 220 A. According to the calculation formulas [30], the amount of material wear is inversely proportional to the hardness of the material under the same external conditions. thus, the coating at the melting current of 220 A has a larger amount of wear.

To further investigate the effect of the melting current on the wear resistance of the coating, the wear morphologies of the substrate and the FeCrMnCuNiSi$_1$ high-entropy alloy coatings were observed and analyzed. Figure 7 shows the SEM images of the wear morphologies of the base material and the high-entropy alloy coatings at different melting currents. A large area of dark-colored flakes within the substrate abrasion marks can be found in Figure 7a. A further magnified Figure 7b shows that the abrasion flakes are nearly fan-shaped or flaky, and exhibit warped boundaries, which lead to the large craters after the abrasion flakes. This is because the coating surface is subjected to cyclic contact stress; the maximum shear stress is at a certain depth under the surface. When the surface strength is insufficient, fatigue cracks will be generated, at which time the maximum shear stress will extend to the surface along the plastic deformation, resulting in spalling of the surface material, which is characteristic of fatigue wear. At the same time, the contact surface temperature is high, and it is easy to produce an oxide layer because of the cyclic effect of stress, which can be proved by the EDS analysis of point 1 in Figure 7c. The oxygen content of point 1 reaches 15.5%, which is shown in Table 3. It can be concluded that the wear mechanism is typical of an oxide layer.

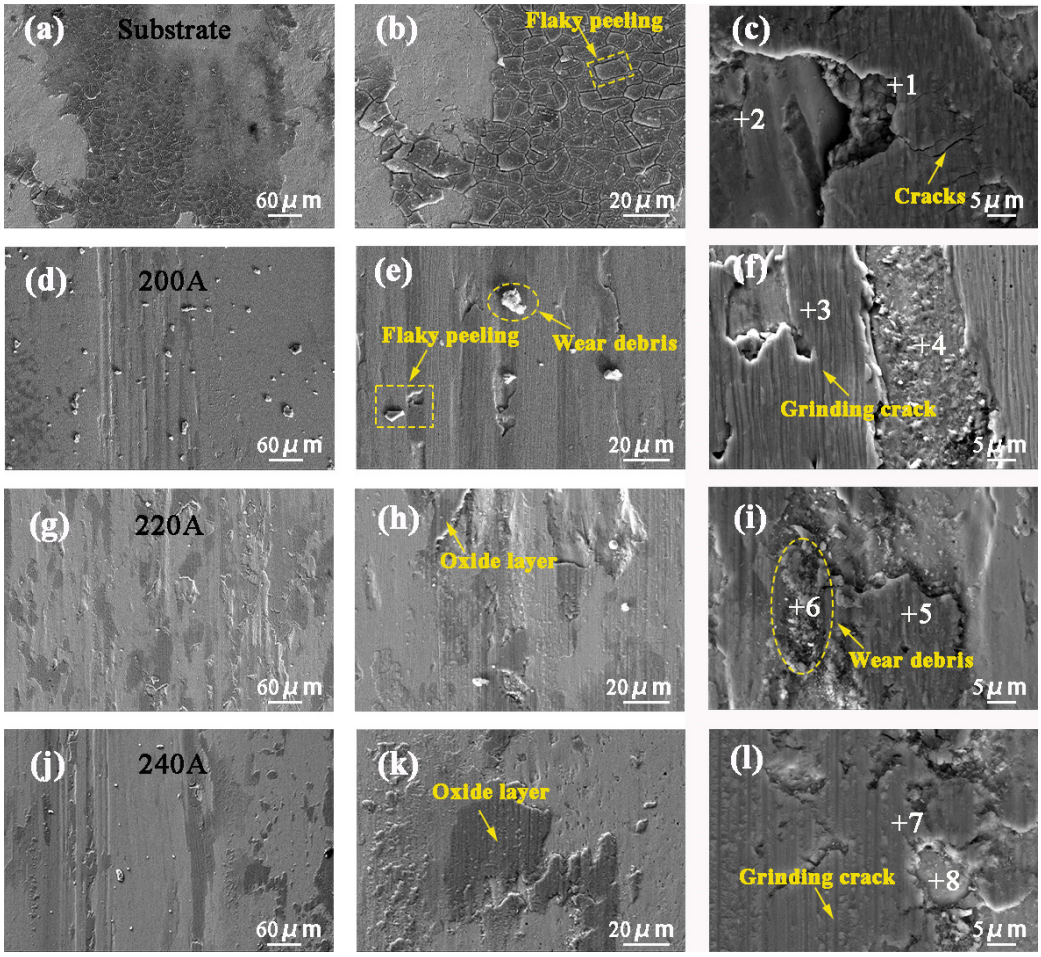

Figure 7. SEM images of the wear morphology of the 40Cr and FeCrMnCuNiSi$_1$ high-entropy alloy coatings at different melting currents. (**a**–**c**) Substrate; (**d**–**f**) 200 A; (**g**–**i**) 220 A; (**j**–**l**) 240 A.

Table 3. EDS of the friction and wear scar structures of the FeCrMnCuNiSi$_1$ high-entropy alloy coating under the substrate and different cladding currents.

Sample	Point	Fe	Cr	Mn	Cu	Ni	Si
40Cr	1	80.3	15.5	1.4	1.4	0.9	0.2
	2	96.2	0	1.9	1.0	0.7	0
200A	3	60.3	7.9	0.9	7.6	8.1	6.5
	4	67.1	0.6	1.3	7.4	8.5	6.3
220A	5	57.2	17.1	1.1	5.8	7.7	4.2
	6	66.2	1.9	1.2	5.4	8.1	7.4
240A	7	53.6	13.9	1.1	9.0	8.2	5.8
	8	66.3	0	1.2	8.6	7.3	5.4

It can be seen from Figure 7g that there is a relatively flat and smooth adhesion layer on the wear track of the coating at 220 A. It is in the same direction as the reciprocal sliding of the grinding ball, from which it can be concluded that the adhesion layer is a layer produced by the plastic deformation of the coating surface material caused by the applied load and shear stress. There are pits on the surface of the coating, as shown in Figure 7h. This may be caused by cracks in the stress concentration area of the surface layer of the coating under the cycling action of Si_3N_4, after which the cracks can extend to the surface and peel off to form pits. An EDS analysis of points 5 and 6 in Figure 7i, shown in Table 3, revealed that the oxygen content at point 5 was significantly higher than that of point 6, which reached 17.1%; thus, the dark adherent layer on the wear path of the coating at

220 A was judged to be an oxide layer. From the above, it is known that the coating has a high Si content at the melting current of 220 A. An oxide layer with a high Si content is easy to break and adhere to the surface of the Si_3N_4 grinding balls by an atomic bonding reaction under local stress (cold welding), resulting in a large amount of wear on the coating surface. Therefore, the wear mechanism of the coating at 220 A is adhesive wear. Uniformly scattered granular abrasive chips are found in the wear tracks of the coating at 200 A and 240 A, as shown in Figure 7d,j. More grooves of varying depths are also found on the wear surface, which were caused by the plowing action of the Si_3N_4 grinding balls. It is judged that these two coatings produce abrasive wear on the surface. The EDS results of Figure 7f,l are shown in Table 3. The oxygen content of the surface layer is much higher than that of the crater coating; thus, the surface layer undergoes oxidative wear. The shift in the wear mechanism of the coating exists because of the high microhardness of the coating at the melting currents of 200 A and 240 A. A non-material transfer of abrasive chips on the wear surface occurs, and the frictional heat promotes the oxidation of the microscopic abrasive chips, which eventually form an oxide layer under the continuous grinding of the Si_3N_4 grinding balls. Figure 7j,k show the presence of a larger oxide layer in the area on the wear surface at the melting current of 240 A.

Combined with the surface element distribution analysis in Figure 8, it can be observed that the oxide layer within the wear marks of this parameter is flat and dense, and the dense oxide layer in the high-entropy alloy coating is beneficial to the improvement of the wear resistance of the coating [31].

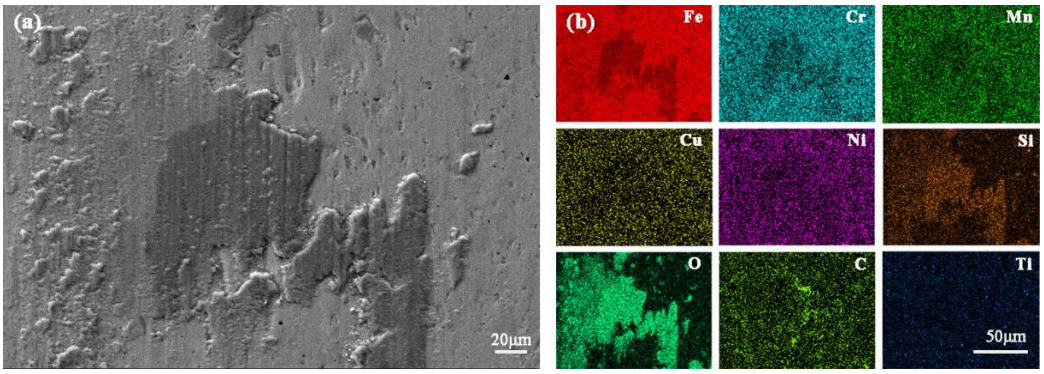

Figure 8. Wear morphology and surface element distribution of the high-entropy alloy coating at a melting current of 240 A. (**a**) Wear marks SEM; (**b**) Wear marks EDS surface scan.

4. Conclusions

By investigating the effect of the tungsten electrode melting current on the microstructure and wear resistance of the $FeCrMnCuNiSi_1$ coating, the process parameters of the coating prepared by the $FeCrMnCuNiSi_1$ high-entropy powder-core wire were obtained, and the microstructure, microhardness, and wear resistance of the coatings were studied. The main conclusions can be obtained as follows:

1. When the melting current is 200 A, the coating shows a single BCC structure. When the melting current is 220 A and 240 A, the coating is a mixed phase of FCC and BCC. When the melting current is 220 A, the coating microstructure is a coarse columnar crystal. When the melting current is 200 A and 240 A, the coating microstructure is a fine equiaxed crystal.
2. The coating has the highest average microhardness of 689.73 HV at a melting current of 200 A, which is twice the average hardness of the base material. As the current increases, the average microhardness of the coating decreases significantly with the decrease in Cr segregation in the coating and the generation of the Si-containing FCC phase.
3. The wear resistance of the coating is weakest at 220 A, which is only 1/3 of the maximum wear depth of the base material. The cross-sectional area of the abra-

sion marks is 1/5 of the cross-sectional area of the base material. The wear rate is 6168.82 $\mu m^3/(N \cdot \mu m)$, which is only 22% of the wear rate of the base material. The wear mechanism of the coating at 220 A is mainly adhesive wear and oxidation wear. When the melting current is 200 A, the prepared high-entropy alloy coatings have good wear resistance and meet the practical production requirements.

Author Contributions: Conceptualization, X.S. and M.C.; methodology, W.L.; formal analysis, X.S.; investigation, X.S.; resources, W.L.; writing—original draft preparation, X.S.; writing—review and editing, M.C. and W.L.; supervision, W.L.; project administration, W.L.; funding acquisition, W.L. All authors have read and agreed to the published version of the manuscript.

Funding: National Natural Science Foundation of China (Grant No. 51975264); Natural Science Foundation of the Jiangsu Higher Education Institutions of China (Grant No. 19KJD430004); Jiangsu University of Technology Graduate Student Practice Innovation Program (Grant No. XSJCX21_10).

Data Availability Statement: Not applicable.

Acknowledgments: The authors thank the Jiangsu Key Laboratory of Advanced Material Design and Additive Man-ufacturing for providing equipment support.

Conflicts of Interest: The authors declare that they have no known competing financial interest or personal relationships that could have appeared to influence the work reported in this paper.

References

1. George, E.P.; Raabe, D.; Ritchie, R.O. High-entropy alloys. *Nat. Rev. Mater.* **2019**, *4*, 515–534. [CrossRef]
2. Yeh, J.W.; Chen, S.K.; Lin, S.J.; Gan, J.Y.; Chin, T.S.; Shun, T.T.; Tsau, C.H.; Chang, S.Y. Nanostructured high-entropy alloys with multiple principal elements: Novel alloy design concepts and outcomes. *Adv. Eng. Mater.* **2004**, *6*, 299–311. [CrossRef]
3. Cantor, B.; Chang, I.; Knight, P.; Vincent, A. Microstructural development in equiatomic multicomponent alloys. *Mater. Sci. Eng. A.* **2004**, *375–377*, 213–218. [CrossRef]
4. Zhang, C.; Zhu, J.K.; Ji, C.Y.; Guo, Y.Z.; Fang, R.; Mei, S.W.; Liu, S. Laser powder bed fusion of high-entropy alloy particle-reinforced stainless steel with enhanced strength, ductility, and corrosion resistance. *Mater. Des.* **2021**, *209*, 109950. [CrossRef]
5. Prabhu, T.R.; Arivarasu, M.; Chodancar, Y.; Arivazhagan, N.; Sumanth, G.; Mishra, R.K. Tribological Behaviour of Graphite-Reinforced FeNiCrCuMo High-Entropy Alloy Self-Lubricating Composites for Aircraft Braking Energy Applications. *Tribol. Lett.* **2019**, *67*, 78–93. [CrossRef]
6. Muangtong, P.; Rodchanarowan, A.; Chaysuwan, D.; Chanlek, N.; Goodall, R. The corrosion behaviour of CoCrFeNi-x (x = Cu, Al, Sn) high entropy alloy systems in chloride solution. *Corros. Sci.* **2020**, *172*, 108740. [CrossRef]
7. Zhou, Y.J.; Zhang, Y.; Wang, Y.L.; Chen, G.L. Solid solution alloys of $AlCoCrFeNiTi_x$ with excellent room-temperature mechanical properties. *Appl. Phys. Lett.* **2007**, *90*, 181904. [CrossRef]
8. Moghaddam, A.O.; Sudarikov, M.; Shaburova, N.; Zherebtsov, D.; Zhivulin, V.; Solizoda, I.A.; Starikov, A.; Veselkov, S.; Samoilova, O.; Trofimov, E. High temperature oxidation resistance of W-containing high-entropy alloys. *J. Alloys Compd.* **2022**, *897*, 162733. [CrossRef]
9. Jin, B.Q.; Zhang, N.N.; Zhang, Y.; Li, D.Y. Microstructure, phase composition and wear resistance of low valence electron concentration $Al_xCoCrFeNiSi$ high-entropy alloys prepared by vacuum arc melting. *J. Iron. Steel. Res. Int.* **2021**, *28*, 181–189. [CrossRef]
10. Campari, E.G.; Casagrande, A.; Colombini, E.; Gualtier, M.L.; Veronesi, P. The Effect of Zr Addition on Melting Temperature, Microstructure, Recrystallization and Mechanical Properties of a Cantor High-entropy Alloy. *Materials* **2021**, *14*, 5994. [CrossRef] [PubMed]
11. Nam, S.; Lee, H.W.; Jung, I.H.; Kim, Y.M. Microstructural Characterization of TiC-Reinforced Metal Matrix Composites Fabricated by Laser Cladding Using FeCrCoNiAlTiC High-entropy Alloy Powder. *Appl. Sci.* **2021**, *11*, 6580. [CrossRef]
12. Hruška, P.; Lukáč, F.; Cichoň, S.; Vondráček, M.; Čížek, J.; Fekete, L.; Lančok, J.; Veselý, J.; Minárik, P.; Cieslar, M.; et al. Oxidation of amorphous HfNbTaTiZr high-entropy alloy thin films prepared by DC magnetron sputtering. *J. Alloys Compd.* **2021**, *869*, 157978. [CrossRef]
13. Arif, Z.U.; Khalid, M.Y.; Rehman, E.U.; Ullah, S.; Tariq, A. A review on laser cladding of high-entropy alloys, their recent trends and potential applications. *J. Manuf. Process.* **2021**, *68*, 225–273. [CrossRef]
14. Fujieda, T.; Shiratori, H.; Kuwabara, K.; Kato, T.; Yamanaka, K.; Koizumi, Y.; Chiba, A. First demonstration of promising selective electron beam melting method for utilizing high-entropy alloys as engineering materials. *Mater. Lett.* **2015**, *159*, 12–15. [CrossRef]
15. Gao, P.; Fu, R.; Liu, J.; Chen, B.; Zhang, B.; Zhao, D.; Yang, Z.; Guo, Y.C.; Liang, M.X.; Li, J.P.; et al. Influence of Plasma Arc Current on the Friction and Wear Properties of CoCrFeNiMn High-entropy Alloy Coatings Prepared on CGI through Plasma Transfer Arc Cladding. *Coatings* **2022**, *12*, 633. [CrossRef]
16. Fan, Q.K.; Chen, C.; Fan, C.L.; Liu, Z.; Cai, X.Y.; Lin, S.B.; Yang, C.L. Ultrasonic suppression of element segregation in gas tungsten arc cladding AlCoCuFeNi high-entropy alloy coatings. *Surf. Coat. Technol.* **2021**, *420*, 127364. [CrossRef]

17. Duriagina, Z.; Kulyk, V.; Kovbasiuk, T.; Vasyliv, B.; Kostryzhev, A. Synthesis of Functional Surface Layers on Stainless Steels by Laser Alloying. *Metals.* **2021**, *11*, 434. [CrossRef]
18. Duriagina, Z.; Kovbasyuk, T.; Kulyk, V.; Trostianchyn, A.; Tepla, T. *Technologies of High-Temperature Insulating Coatings on Stainless Steels*; Engineering Steels and High Entropy-Alloys; IntechOpen: London, UK, 2020; pp. 57–80.
19. Shen, Q.K.; Kong, X.D.; Chen, X.Z. Fabrication of bulk Al-Co-Cr-Fe-Ni high-entropy alloy using combined cable wire arc additive manufacturing (CCW-AAM): Microstructure and mechanical properties. *J. Mater. Sci. Technol.* **2021**, *74*, 136–142. [CrossRef]
20. Dong, B.S.; Wang, Z.Y.; Pan, Z.X.; Muránsky, O.; Shen, C.; Reid, M.; Wu, B.T.; Chen, X.Z.; Li, H.J. On the development of pseudo-eutectic AlCoCrFeNi$_{2.1}$ high entropy alloy using Powder-bed Arc Additive Manufacturing (PAAM) process. *Mat. Sci. Eng. A–Struct.* **2021**, *802*, 140639. [CrossRef]
21. Fan, Q.K.; Chen, C.; Fan, C.L.; Liu, Z.; Cai, X.Y.; Lin, S.B.; Yang, C.L. Ultrasonic induces grain refinement in gas tungsten arc cladding AlCoCrFeNi high-entropy alloy coatings. *Mat. Sci. Eng. A–Struct.* **2021**, *821*, 141607. [CrossRef]
22. Sokkalingam, R.; Muthupandi, V.; Sivaprasad, K.; Prashanth, K.G. Dissimilar welding of $Al_{0.1}$CoCrFeNi high-entropy alloy and AISI304 stainless steel. *J. Mater. Res.* **2019**, *34*, 2683–2694. [CrossRef]
23. Shen, Q.K.; Xue, J.X.; Yu, X.Y.; Zheng, Z.H.; Ou, N. Triple-wire plasma arc cladding of Cr-Fe-Ni-Ti$_x$ high-entropy alloy coatings. *Surf. Coat. Technol.* **2022**, *443*, 128638. [CrossRef]
24. Cheng, J.B.; Sun, B.; Ge, Y.Y.; Hu, X.L.; Zhang, L.H.; Liang, X.B.; Zhang, X.C. Effect of B/Si ratio on structure and properties of high-entropy glassy $Fe_{25}Co_{25}Ni_{25}(B_xSi_{1-x})_{25}$ coating prepared by laser cladding. *Surf. Coat. Technol.* **2020**, *402*, 126320. [CrossRef]
25. Chao, Q.; Guo, T.; Jarvis, T.; Wu, X.H.; Hodgson, P.; Fabijanic, D. Direct Laser Deposition Cladding of Al_xCoCrFeNi High-entropy Alloys on a High-temperature Stainless Steel. *Surf. Coat. Technol.* **2017**, *332*, 440–451. [CrossRef]
26. Middleburgh, S.C.; King, D.M.; Lumpkin, G.R.; Cortie, M.; Edwards, L. Segregation and migration of species in the CrCoFeNi high-entropy alloy. *J. Alloys Compd.* **2014**, *599*, 179–182. [CrossRef]
27. Zhang, G.J.; Tian, Q.W.; Yin, K.X.; Niu, S.Q.; Wu, M.H.; Wang, W.W.; Wang, Y.N.; Huang, J.C. Effect of Fe on microstructure and properties of AlCoCrFe$_x$Ni(x = 1.5,2.5) high-entropy alloy coatings prepared by laser cladding. *Intermetallics* **2020**, *119*, 106722. [CrossRef]
28. Wang, H.B.; Gee, M.; Qiu, Q.F.; Zhang, H.; Liu, X.M.; Nie, H.B.; Song, X.Y.; Nie, Z.R. Grain size effect on wear resistance of WC-Co cemented carbides under different tribological conditions. *J. Mater. Sci. Technol.* **2019**, *35*, 2435–2446. [CrossRef]
29. Jin, B.Q.; Zhang, N.N.; Yu, H.S.; Hao, D.X.; Ma, Y.L. Al_xCoCrFeNiSi high-entropy alloy coatings with high microhardness and improved wear resistance. *Surf. Coat. Technol.* **2020**, *402*, 126328. [CrossRef]
30. Archard, J.F. Contact and rubbing of flat surfaces. *J. Appl. Phys.* **1953**, *24*, 981–988. [CrossRef]
31. Liu, C.; Li, Z.; Lu, W.; Bao, Y.; Xia, W.Z.; Wu, X.X.; Zhao, H.; Gault, B.; Liu, C.L.; Herbig, M.; et al. Reactive wear protection through strong and deformable oxide nanocomposite surfaces. *Nat. Commun.* **2021**, *12*, 5518. [CrossRef]